Engineering Geology 234 (2018) 55–64

Contents lists available at ScienceDirect

Engineering Geology

journal homepage: www.elsevier.com/locate/enggeo

# Numerical investigation of water evaporation from Fontainebleau sand in an environmental chamber

Ni An[a], Sahar Hemmati[b], Yu-jun Cui[a,*], Chao-sheng Tang[c]

[a] Ecole des Ponts ParisTech, Laboratoire Navier/CERMES, 6 – 8 av. Blaise Pascal, Cité Descartes, Champs sur Marne, 77455 Marne la Vallée, France
[b] IFSTTAR – French Institute of Science and Technology for Transport, Development and Networks, 77447 Marne la Vallée, France
[c] Nanjing University, School of Earth Sciences and Engineering, 163 Xianlin Road, Nanjing 210093, China

ARTICLE INFO

*Keywords:*
Evaporation
Environmental chamber tests
Fontainebleau sand
Numerical modelling
Soil-atmosphere interaction

ABSTRACT

The global warming and climate change have aroused increasing attention to the effect of intensive soil water evaporation on earth constructions. When investigating the hydro-mechanical behavior of soil during evaporation, it is of paramount importance to consider the coupled transport of heat and water in soil. In this study, four different evaporation tests of Fontainebleau sand conducted in an environmental chamber are investigated. A numerical approach combing a coupled hydro-thermal model and a soil-atmosphere interaction model is adopted, enabling the numerical estimation of soil temperature and soil water content variations. Comparison between the measurements and the simulation results shows the relevance of the proposed approach with consideration of suitable thermal and hydraulic boundary conditions and soil parameters. Further inspection on the variations of soil water content and soil temperature suggests the significant influence of water and heat flux boundary conditions at the soil-atmosphere interface. In this study, it is proposed to estimate the mode of soil temperature variations directly based on the observed actual evaporation curve. Moreover, the simulation results also reveal the necessity of accounting for the dry layer formed in sand during evaporation.

## 1. Introduction

In the context of global warming and climate change, the effect of intensive evaporation during drought periods on soil hydro-thermal-mechanical behavior and the corresponding response of building foundations and earth constructions has aroused more and more attention. In literature, it was investigated that the performance of the soil cover system for waste disposal (Wilson et al., 1993; Yanful et al., 1999, 2003; Yanful and Choo, 1997; Yang and Yanful, 2002; Swanson et al., 2003; Gerard et al., 2008), the pore-water pressure distribution within tailings impoundment (Rykaart et al., 2001) and the seepage in soils (Gitirana Jr., 2005; Gitirana et al., 2006; Gerard et al., 2008; Leung and Ng, 2013) were greatly affected by evaporation process. Besides, soil desiccation cracks and settlement can also be observed during evaporation, in particular for clayey soils (Rayhani et al., 2007; Ta, 2009; Tang et al., 2010, 2011, 2012; Song et al., 2013, 2014; Song, 2014). Rahardjo et al. (2013) indicated that most problems related to evaporation are mainly caused by the increase of negative pore-water pressure along with the decrease of soil water content during the drying process. As a consequence, it is essential to consider soil water evaporation in the study of the hydro-mechanical behavior of geotechnical and geo-environmental structures.

Many researchers have experimentally studied the soil water evaporation and its effect on soil hydro-mechanical behavior (Wilson, 1990; Kondo et al., 1992; Yang and Yanful, 2002; Lee et al., 2003; Yamanaka et al., 2004; Rayhani et al., 2007; Tang et al., 2010, 2011, 2012; Smits et al., 2011). Wilson (1990) performed simple column drying tests and observed that soil temperature went down initially in a short period and then started to increase in the following period, while a constant increase was identified in the test by Smits et al. (2011). It is concluded that soil temperature evolution was related intimately to the air condition. On the other hand, soil volumetric water content decreased more quickly in the region near the soil surface in comparison with the deeper region due to the evaporation at soil surface. In the study of soil desiccation cracks (Rayhani et al., 2007; Tang et al., 2010, 2011, 2012), the influences of soil volumetric water content, suction and tensile strength were investigated in depth but the effect of heat flux was scarcely mentioned, even though it is widely recognized that water vapor transfer is closely coupled to the heat transfer in the near soil-atmosphere interface region (Philip and De Vries, 1957; Wilson, 1990; Thomas and King, 1991; Grifoll et al., 2005; Cui et al., 2005, 2010; Bittelli et al., 2008). Basically, the water and heat transfers may

* Corresponding author.
*E-mail address:* yu-jun.cui@enpc.fr (Y.-j. Cui).

https://doi.org/10.1016/j.enggeo.2018.01.005
Received 1 October 2017; Received in revised form 4 January 2018; Accepted 4 January 2018
Available online 05 January 2018
0013-7952/ 

affect the volume change behavior of soils due to the coupled hydro-thermal-mechanical process. Nevertheless, soil volume change behavior can be neglected in some circumstances. For instance, in the case of sand or lime/cement treated soils (An, 2017).

Different models were proposed to study the coupled hydro-thermal behavior of soils during evaporation process (Wilson, 1990; Kondo et al., 1992; Wilson et al., 1994; Hansson et al., 2005; Grifoll et al., 2005; Bittelli et al., 2008; Smits et al., 2011). However, the heat and water flows in soil were not fully coupled in these models. For instance, a numerical model for heat, water vapor and liquid water fluxes in soil was developed by Bittelli et al. (2008), and was proved to be consistent with experimental measurements. Nevertheless, the model developed is a simple coupled hydro-thermal model because the soil hydraulic head and temperature do not interact synchronously. Therefore, the water and heat transfers in soil were not considered as fully coupled, limiting the wide application of this kind of models.

It is thus indispensable to consider a fully coupled hydro-thermal model to well estimate the variations of soil temperature and volumetric water content. In this study, a numerical approach combining a fully coupled hydro-thermal model and a soil-atmosphere interaction model is adopted to study the coupled hydro-thermal behavior of soil during evaporation. Four different evaporation tests with recording soil hydro-thermal behavior in an environmental chamber conducted by Song et al. (2013, 2014) and Song (2014) are considered to verify the proposed approach in the specific laboratory conditions. The numerical modelling is conducted through the FreeFem + + code (Hecht, 2010) with Finite Element Method. Moreover, the variations of soil temperature and volumetric water content in four evaporation tests are further discussed, suggesting the significant influences of water and heat flux boundary conditions.

## 2. Coupled hydro-thermal model

Generally, non-isothermal unsaturated soil consists of three basic phases: solid grains, water and air. Specially, the water phase is composed of liquid and vapor. Meantime, the water vapor transfer is closely coupled to the thermal process. In this numerical modelling, several assumptions are made, as follows:

i) The solid phase is considered as a continuous medium and no volume change occurs;
ii) The liquid flow is considered to be incompressible, and osmotic suction is neglected;
iii) The temperatures of soil grains, water and air are assumed to keep an equilibrium state, owning the same value at the same point;
iv) The air pressure keeps constant during the studied period thus the air flow is not considered.

### 2.1. Water transfer

The non-isothermal liquid flow in unsaturated soils is described by Darcy's law as:

$$\mathbf{q}_l = -K\rho_l \nabla(\varphi + y) \tag{1}$$

where $\mathbf{q}_l$ (kg/(sm$^2$)) is the flux density of liquid; $K$ (m/s) is the hydraulic conductivity of unsaturated soil; $\rho_l$ (kg/m$^3$) is the liquid density; $\varphi$ (m) is the hydraulic head; $y$ (m) is the elevation above a nominal datum.

It has been considered that the pore vapor flux in unsaturated soil takes place due to two main effects: the bulk flow of pore air and the molecular diffusion. In this study, without considering the effect of bulk flow, the pore vapor flux can be presented as (Philip and De Vries, 1957; Wilson, 1990):

$$\mathbf{q}_v = -D_{atm}\alpha\beta\nabla\rho_v \tag{2}$$

where $\mathbf{q}_v$ (kg/(sm$^2$)) is the flux density of vapor; $D_{atm}$ (m$^2$/s) is the molecular diffusivity of vapor in the air; $\alpha$ is the tortuosity factor for soil, equal to $\beta^{2/3}$; $\beta$ is the cross-sectional area of soil that is available for vapor flow (i.e., (1 − S)n); the vapor density $\rho_v$ (kg/m$^3$) in a system with a thermodynamic equilibrium between the liquid and vapor phases is estimated as (Philip and De Vries, 1957):

$$\rho_v = \rho_0 \exp(\varphi g M_w / RT) \tag{3}$$

where $\rho_0$ (kg/m$^3$) is the saturated water vapor density (Thomas and King, 1991):

$$\rho_0 = \{194.4\exp[-0.06374(T-273) + 0.1634\times10^{-3}(T-273)^2]\}^{-1} \tag{4}$$

The flux density of vapor can be rewritten as:

$$\mathbf{q}_v = -\rho_l(D_{\varphi v}\nabla\varphi + D_{Tv}\nabla T) \tag{5}$$

where,

$$D_{\varphi v} = \frac{D_{atm}\alpha\beta\rho_0 h g M_W}{RT\rho_l} \tag{6}$$

$$D_{Tv} = \frac{D_{atm}\alpha\beta}{\rho_l}\left(-\frac{\rho_0 h\varphi g M_W}{RT^2} + h\frac{\partial\rho_0}{\partial T}\right) \tag{7}$$

where, $D_{\varphi v}$ and $D_{Tv}$ represent isothermal vapor diffusivity (m/s) and thermal vapor diffusivity (m$^2$/(sK)), respectively. Both of them are related to soil temperature and hydraulic head/moisture content. Additionally, the mass transfer of water is the sum of liquid and vapor flows:

$$\mathbf{q} = \mathbf{q}_l + \mathbf{q}_v \tag{8}$$

The conservation equation of water mass is written as:

$$\frac{\partial w}{\partial t} = -\nabla\cdot\mathbf{q} \tag{9}$$

where the moisture content $w$ (kg/m$^3$) can be expressed by both the vapor and liquid parts:

$$w = \theta\rho_l + (n-\theta)\rho_v \tag{10}$$

By substituting Eqs. (1) and (5) into Eqs. (8) and (9), the governing equation for water mass transfer is obtained:

$$C_\varphi\frac{\partial\varphi}{\partial t} + C_{\varphi T}\frac{\partial T}{\partial t} = \nabla\cdot[K_\varphi\nabla\varphi] + \nabla\cdot[K_{\varphi T}\nabla T] + \rho_l\nabla K \tag{11}$$

where,

$$C_\varphi = (\rho_l - \rho_v)\frac{\partial\theta}{\partial\varphi} + (n-\theta)\frac{\rho_0 h g M_W}{RT} \tag{12}$$

$$C_{\varphi T} = (n-\theta)\left(-\frac{\rho_0 h\varphi g M_W}{RT^2} + h\frac{\partial\rho_0}{\partial T}\right) \tag{13}$$

$$K_{\varphi T} = \rho_l D_{Tv} \tag{14}$$

$$K_\varphi = \rho_l D_{\varphi v} + K\rho_l \tag{15}$$

### 2.2. Heat transfer

Generally, thermal conduction in soil is in accordance with Fourier's law. Latent heat represents the heat consumed for vapor-liquid transfer. Considering conduction and latent heat transfer as the primary heat transmission mechanisms, energy flux can be expressed as:

$$\mathbf{Q} = -\lambda\nabla T + L_v\mathbf{q}_v \tag{16}$$

where $\mathbf{Q}$ (W/m$^2$) is the transferred heat flux through soil-atmosphere interface; λ (W/(mK)) is the soil thermal conductivity; $L_v$ (J/kg) is the specific latent heat of vaporization.

Further, Eq. (16) can be extended as:

$$\begin{aligned}\mathbf{Q} &= -\lambda\nabla T + L_v[-\rho_l(D_{\varphi v}\nabla\varphi + D_{Tv}\nabla T)] \\ &= -(\lambda + L_v\rho_l D_{Tv})\nabla T - L_v\rho_l D_{\varphi v}\nabla\varphi\end{aligned} \tag{17}$$

The conservation equation of heat energy can be expressed as:

$$\frac{\partial(\Phi)}{\partial t} = -\nabla\cdot\mathbf{Q} \tag{18}$$

where $\Phi = CT + (n - \theta)L_v\rho_v$.

Thus, the governing equation of heat flow is expressed as:

$$C_T\frac{\partial T}{\partial t} + C_{T\varphi}\frac{\partial \varphi}{\partial t} = \nabla\cdot[K_T\nabla T] + \nabla\cdot[K_{T\varphi}\nabla\varphi] \tag{19}$$

where,

$$C_T = C + (n - \theta)L_v\frac{\partial \rho_v}{\partial T} \tag{20}$$

$$C = \rho_s C_{ps}(1 - n) + \rho_l C_{pl}\theta + \rho_v C_{pv}(n - \theta) + \rho_a C_{pa}(n - \theta) \tag{21}$$

$$C_{T\varphi} = (n - \theta)L_v\frac{\partial \rho_v}{\partial \varphi} - L_v\rho_v\frac{\partial \theta}{\partial \varphi} \tag{22}$$

$$K_T = \lambda + L_v\rho_l D_{Tv} \tag{23}$$

$$K_{T\varphi} = L_v\rho_l D_{\varphi v} \tag{24}$$

In this study, the governing Eqs. (11) and (19) for mass and energy transfers respectively are used to study the soil coupled hydro-thermal behavior during evaporation through the FreeFem + + code (Hecht, 2010) with Finite Element Method. More details about the equation transformations can be found in An (2017).

## 3. Environmental chamber tests

### 3.1. Environmental chamber introduction

A large-scale environmental chamber was designed by Song (2014) and Cui et al. (2013) in the laboratory with a stable ambient temperature (about 20 °C). The whole experimental chamber consists of a chamber, a wind supply unit, an air collection unit, a photograph collection unit, a water supply unit and a data logging system. The chamber owns a top cover of 8 mm thick, walls of 20 mm thick, an internal width of 800 mm and an internal length of 1000 mm.

During the sample preparation by compaction in the chamber, different sensors were installed at various depths to monitor the variations of soil temperature and volumetric water content during a test (Song et al., 2013, 2014; Song, 2014). Theta Probes were adopted to record the variations of soil volumetric water content, and they were installed at different depths (25 mm, 40 mm, 55 mm, 125 mm and 225 mm below the soil surface). Six PT1000 sensors were buried every 50 mm along the soil column (25 mm, 75 mm, 125 mm, 175 mm, 225 mm and 275 mm beneath the soil surface) to record soil temperature variations. In addition, soil surface temperature was monitored continuously by an infrared thermometer fixed at the top of environmental chamber. At different heights (80 mm, 185 mm, 275 mm, 380 mm and 465 mm) above the soil surface along one side of the wall in the ventilation part, thermistors were installed to record the variations of air temperature. A compacted gravel layer of 15 mm thick (grain diameter: 2–4 mm) was sandwiched between two layers of geotextile of 1 mm thick for the drainage purpose. Meanwhile, two outlets were set up at the bottom of the drainage layer to facilitate soil saturation, drainage and continuous water supply. During the test, air flow rate controlled by a regulator was monitored continuously by a flowmeter. Moreover, wind speed at 50 mm above the center of soil surface was regarded as a representative value in this chamber and was measured by an anemometer fixed on one edge of the chamber.

Various air flow rates and heating tube temperatures were set in four different evaporation tests: with the same temperature in heating tube at 50 °C, Tests 1 and 3 have the air flow rates at 185 and 130 L/min, respectively; holding the same heating tube temperature at 200 °C, Tests 2 and 4 were conducted with air flow rate at 172 and 130 L/min, respectively. Indeed, the air temperature in the environmental chamber is much lower than the heating tube temperature due to heat loss of air in the transport process. The details of these four tests are summarized in Table 1. More details of these four tests can be found in Song et al. (2014).

**Table 1**
Four evaporation tests on Fontainebleau sand (Song et al., 2013, 2014; Song, 2014).

| Test number | Air flow rate (L/min) | Temperature in heating tube (°C) | Test duration (days) |
|---|---|---|---|
| Test 1 | 185 | 50 | 11.5 |
| Test 2 | 172 | 200 | 11.5 |
| Test 3 | 130 | 50 | 17.5 |
| Test 4 | 130 | 200 | 30 |

### 3.2. Soil parameters

As a natural, fine and white siliceous sand, Fontainebleau sand was selected in the evaporation test. Its specific gravity, maximum density and minimum density are 2.64 Mg/m$^3$, 1.75 Mg/m$^3$, and 1.39 Mg/m$^3$, respectively. Its effective grain size $D_{10}$ is 0.14 mm and the coefficient of uniformity, $C_u = D_{60}/D_{10}$, is equal to 1.6 (Delfosse-Ribay et al., 2004). Fig. 1 presents the grain size distribution curve of Fontainebleau sand.

The thermal conductivity for Fontainebleau sand was measured by KD2 analyzer (Tang and Cui, 2007; Buongiorno et al., 2009; Teng et al., 2010). Adopting the method developed by Côté and Konrad (2005) (Table 2), the thermal conductivity of Fontainebleau sand is expressed in an analytical relationship with volumetric water content as:

$$\lambda = (\lambda_{sat} - \lambda_{dry})\cdot\lambda_r + \lambda_{dry} \tag{25}$$

$$\lambda_r = \frac{3.55\cdot S_r}{1 + (3.55 - 1)\cdot S_r} \tag{26}$$

where λ (W/(mK)) is the soil thermal conductivity; $\lambda_{sat}$ and $\lambda_{dry}$ represent the soil volumetric water content in saturated state and dry state, equal to 2.903 (W/(mK)) and 0.276 (W/(mK)), respectively; $\lambda_r$ is the Kersten number; $S_r$ is the degree of saturation. The analytical curve of soil thermal conductivity versus volumetric water content is drawn in Fig. 2. Specifically, the thermal conductivity of the surface region (0 to − 0.025 m) is assumed to be 0.05 (W/(mK)) based on the observed high gradient of soil temperature in this region.

The volumetric water content variations with suction for Fontainebleau sand have been measured by Mbonimpa et al. (2004), Doussan and Ruy (2009), Song (2014) and Song et al. (2013, 2014). The fitting curve of soil water retention is plotted (Fig. 3) depending on van Genuchten model (van Genuchten, 1980) and expressed as:

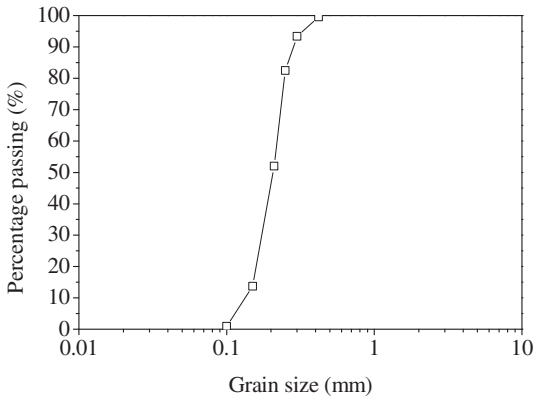


**Fig. 1.** Grain size distribution curve of Fontainebleau sand.

**Table 2**
Soil thermal conductivity (Côté and Konrad, 2005).

$\lambda = (\lambda_{sat} - \lambda_{dry}) \cdot \lambda_r + \lambda_{dry}$

| | | | | |
|---|---|---|---|---|
| $\lambda_{sat}$ | Unfrozen | $\lambda_s^{1-n} \times 0.6^n$ | | |
| | Frozen | $\lambda_s^{1-n} \times 2.24^{n-\theta u} \times 0.6^{\theta u}$ | | |
| $\lambda_r$ | $\frac{\kappa \cdot S_r}{1+(\kappa-1)\cdot S_r}$ | The value of $\kappa$ | Unfrozen | Frozen |
| | | Gravels and coarse sands | 4.60 | 1.70 |
| | | Medium and fine sands | 3.55 | 0.95 |
| | | Silty and clayey soils | 1.90 | 0.85 |
| | | Organic fibrous soils (peat) | 0.60 | 0.25 |
| $\lambda_{dry}$ | $\chi \times 10^{-\eta n}$ | | $\chi$ | $\eta$ |
| | | Cr. rocks and gravels | 1.70 | 1.80 |
| | | Natural mineral soils | 0.75 | 1.20 |
| | | Org. fibrous soils (peat) | 0.30 | 0.87 |

where, $\lambda$ ($Wm^{-1}K^{-1}$) is the soil thermal conductivity; $\lambda_{sat}$ and $\lambda_{dry}$ are the soil volumetric water content in saturated state and dry state, respectively; $\lambda_r$ is the Kersten number; $S_r$ is the degree of saturation; $n$ is the soil porosity; $\theta_u$ is the volume fraction of frozen water; $\kappa$ is the fabric factor to estimate $\lambda_r$; $\chi$ is the material parameter to estimate $\lambda_{dry}$; $\eta$ is the material parameter to estimate $\lambda_{dry}$.

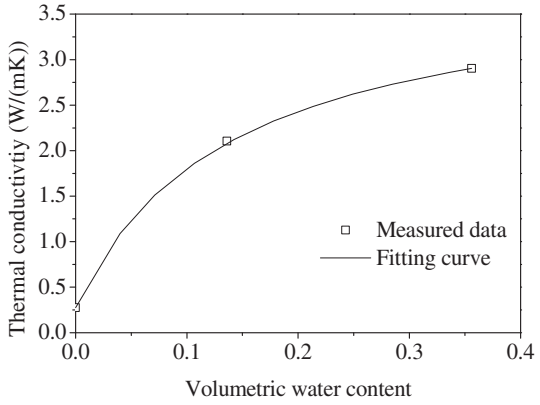


**Fig. 2.** Thermal conductivity versus volumetric water content for Fontainebleau sand.

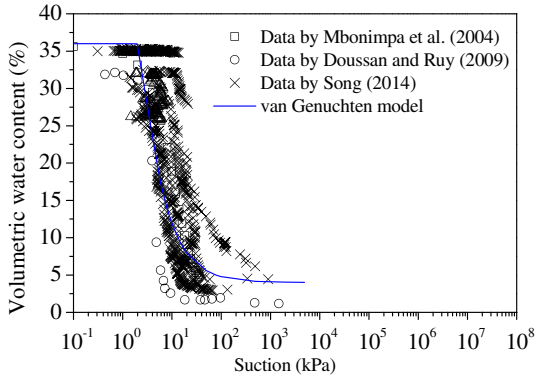


**Fig. 3.** Water retention curve of Fontainebleau sand.

$$S_e = \frac{\theta - \theta_r}{\theta_s - \theta_r} = \left[\frac{1}{1+(\alpha_s \varphi)^n}\right]^m \quad (27)$$

where $S_e$ is the effective saturation; $\theta_s$ is the saturated volumetric water content, equal to 0.356; $\theta_r$ is the residual volumetric water content, equal to 0.04; $\alpha_s$, $m$ and $n$ are the soil constants, equal to 0.4 $kPa^{-1}$, 0.05 and 20, respectively.

In addition, the saturated hydraulic conductivity of Fontainebleau sand was measured through constant head permeability test. Based on the soil water retention curve determined above, the unsaturated hydraulic conductivity of Fontainebleau sand is estimated using van Genuchten model (van Genuchten, 1980) (Fig. 4):

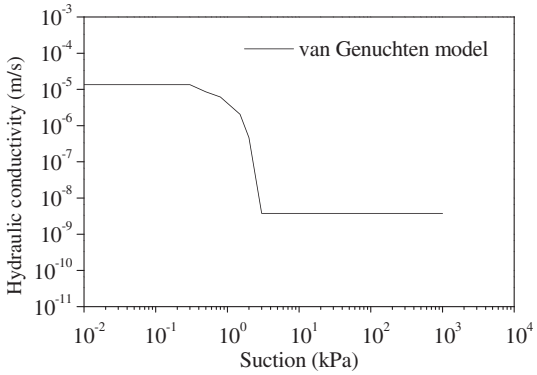


**Fig. 4.** Hydraulic conductivity versus suction for Fontainebleau sand.

$$K = (K_s - K_r)S_e^{0.5}[1-(1-S_e^{1/m})^m]^2 + K_r \quad (28)$$

where the saturated hydraulic conductivity $K_s = 1.36 \times 10^{-5}$ m/s; the residual hydraulic conductivity $K_r = 3.75 \times 10^{-9}$ m/s; other parameters have the same values as in Eq. (27). The hysteresis of soil water retention and hydraulic conductivity variations was not considered in this study.

## 4. Numerical modelling

The two-dimensional numerical model is presented in Fig. 5 with a width of 1 m and a height of 0.3 m. The mesh size is set as 0.02 m × 0.02 m for the numerical calculation. The measured profiles of soil temperature and volumetric water content at the beginning of each test are defined as their initial conditions. At the bottom boundary BC1, soil is assumed to be at saturated state with a stable temperature. No water and heat transfers are considered for the lateral boundaries BC2 and BC4. At the soil-atmosphere interface BC3, the water and heat flux boundary conditions need to estimated depending on the soil-atmosphere interaction model. Specifically, either soil surface temperature or soil heat flux can be used as soil surface thermal boundary condition. They can be selected depending on the academic or engineering purposes and conditions.

In terms of mass balance at the soil surface, the values of rainfall ($P$), runoff ($R_{off}$), interception ($I_{nt}$) and infiltration ($I_{nf}$) are equal to zero in the environmental chamber drying tests. As a result, the evaporation represents the water flux boundary condition at the soil top surface (BC3) in these tests.

Four different drying tests presented in Table 1 were conducted in the environmental chamber. Their evaporation values were calculated by Song (2014):

$$E_a = 86400Q(h_{a-outlet} - h_{a-inlet})/(\rho_l A) \quad (29)$$

where $E_a$ (mm/day) is the actual evaporation rate; $Q$ (L/s) is the air flow rate through the chamber; $h_{a\text{-outlet}}$ and $h_{a\text{-inlet}}$ ($Mg/m^3$) are the absolute humidity values at the outlet and inlet, respectively; $\rho_l$ ($Mg/m^3$) is the water liquid density; $A$ ($m^2$) is the area of the exposed evaporative

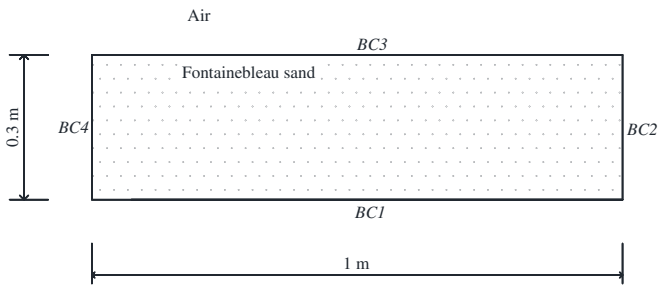


**Fig. 5.** Model dimensions of environmental chamber evaporation tests.

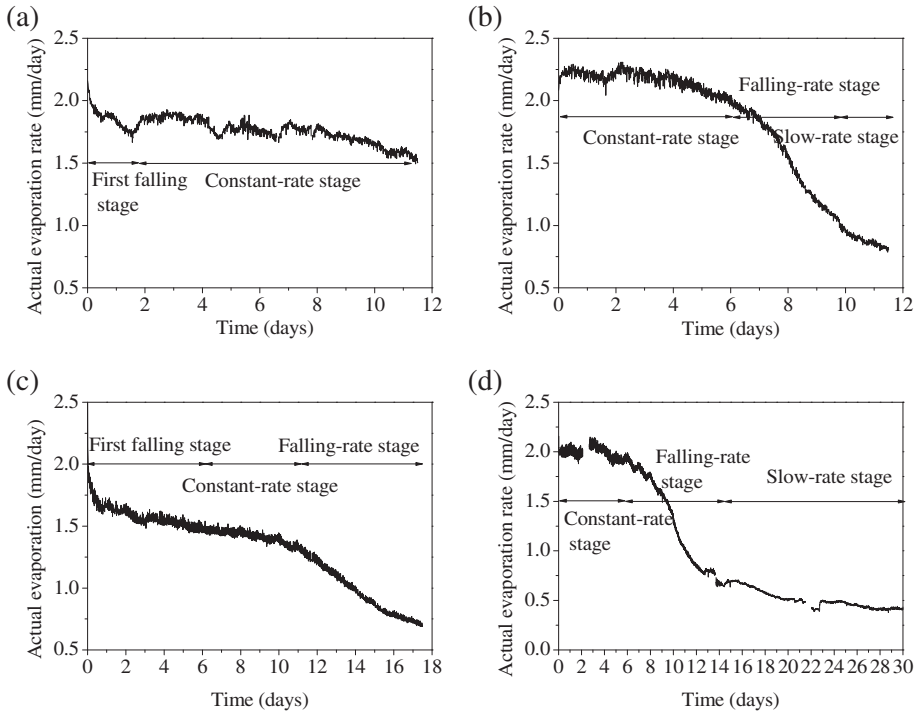


**Fig. 6.** Actual evaporation estimated by Song (2014) in four different tests: (a) Test 1; (b) Test 2; (c) Test 3; (d) Test 4.

surface in the chamber. The four tests last 11.5 days (Fig. 6a), 11.5 days (Fig. 6b), 17.5 days (Fig. 6c) and 30 days (Fig. 6d), respectively.

The energy balance at soil surface was proposed by Blight (1997). Net solar radiation is the sum of soil heat, sensible heat and latent heat fluxes. In this study, the value of net radiation is zero due to the absence of solar radiation in this environmental chamber. As a result, the energy balance is written as:

$$G = H - L_E \tag{30}$$

It shows that the value of soil heat flux $G$ can be determined directly by the values of sensible heat $H$ and latent heat $L_E$. Due to the convection of air flow during soil-atmosphere interaction, the sensible heat ($W/m^2$) can be estimated based on the method proposed by Blight (1997):

$$H = -\rho_a C_{pa} K_H \left(\frac{\partial T}{\partial y}\right)_{air} \tag{31}$$

where $\rho_a$ is the air density, equal to 1.205 $kg/m^3$; $C_{pa}$ is the specific heat capacity of air, equal to 1.0205 J/(kgK); $K_H$ is the eddy diffusivity for heat through air, equal to 100–1000 $m^2/s$ (Zhai and Greatbatch, 2006); $\left(\frac{\partial T}{\partial y}\right)_{air}$ is the vertical temperature gradient in the air, which is estimated depending on the air temperature at a reference level and soil surface temperature.

The latent heat ($Wm^{-2}$) can be estimated by:

$$L_E = \rho_l L_v E_a \tag{32}$$

where $\rho_l$ ($kg/m^3$) is the water liquid density; $L_v$ (J/kg) is the latent heat of water vaporization; the values of actual evaporation $E_a$ (m/s) of four tests were determined and presented in Fig. 6.

Depending on the energy balance, the value of soil heat flux $G$ is then estimated and applied as the heat flux boundary condition on the soil top surface (BC3). All the details of initial conditions and boundary conditions are presented in Table 3. The numerical modelling is performed by finite element code FreeFem + + (Hecht, 2010) using the soil parameters and initial and boundary conditions defined above.

**Table 3**
Initial and boundary conditions.

| Initial conditions | | Measurement data at the starting moment | |
|---|---|---|---|
| | Boundary number | Thermal boundary condition | Hydraulic boundary condition |
| Boundary conditions | BC1 | Soil temperature measured | $U = 0$ |
| | BC2, BC4 | $G = 0$ | $L_{vn} = 0$ |
| | BC3 | $G = H - L_E$<br>$H = f(T_3)$ | $L_{vn} = E_a$ |

Note: $T_3$ means soil temperature at the surface point chosen of "BC3" boundary as shown in Fig. 8.

## 5. Results and analysis

According to the heating tube temperature in the chamber (Table 1), the four tests carried out can be divided into two groups: Group 1 with low air temperature (heating tube temperatures 50 °C) (Test 1 and Test 3) and Group 2 with high air temperature (heating tube temperatures 200 °C) (Test 2 and Test 4).

### 5.1. Test 1 and test 3

Fig. 7a and b present the calculated and measured profiles of soil temperature at different times in Tests 1 and 3, respectively. Overall, the soil temperature in deep region (− 0.025 to − 0.300 m) shows a liner relationship with depth, varying in a small range. In the region near the soil surface (0 to − 0.025 m), the soil temperature increases sharply with depth, presenting a much larger gradient. Thereby, the variations of soil temperature profile can be divided into two parts: near surface region (0 to − 0.025 m) and deep region (− 0.025 to − 0.300 m). On the other hand, it is observed that the soil temperature goes down from the initial moment to reach the minimum value at the second day in Test 1 and the sixth day in Test 3. Afterwards, it begins to go up gradually, showing a temperature rebounding phenomenon during the studied period. Hence, the variations of soil temperature can

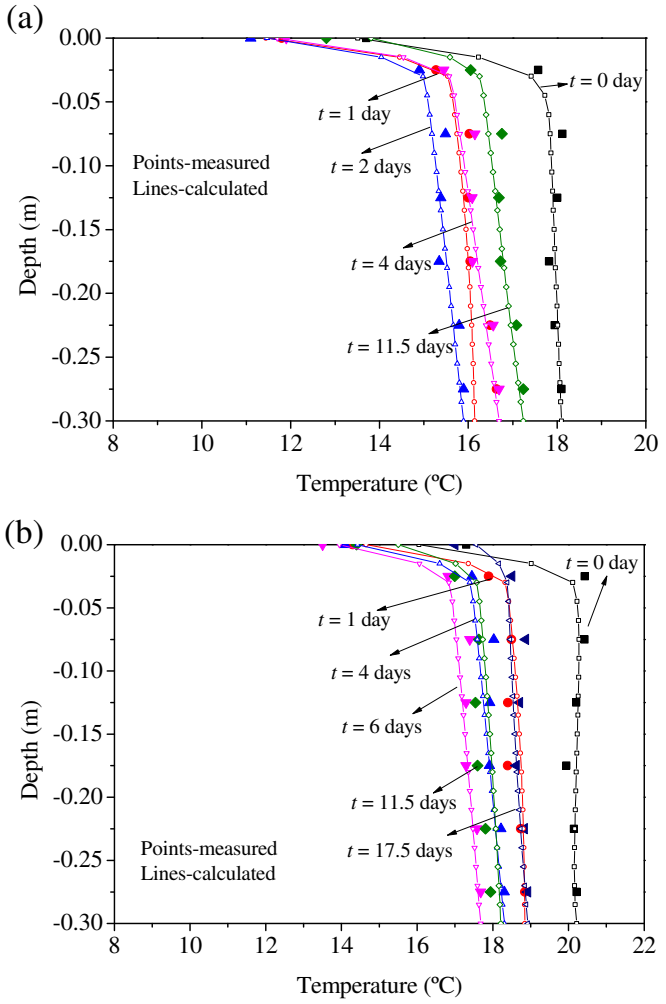


**Fig. 7.** Comparisons between the calculated and measured soil temperature profiles at different moments: (a) at $t$ = 0, 1, 2, 4 and 11.5 days in Test 1; (b) at $t$ = 0, 1, 4, 6, 11.5 and 17.5 days in Test 3.

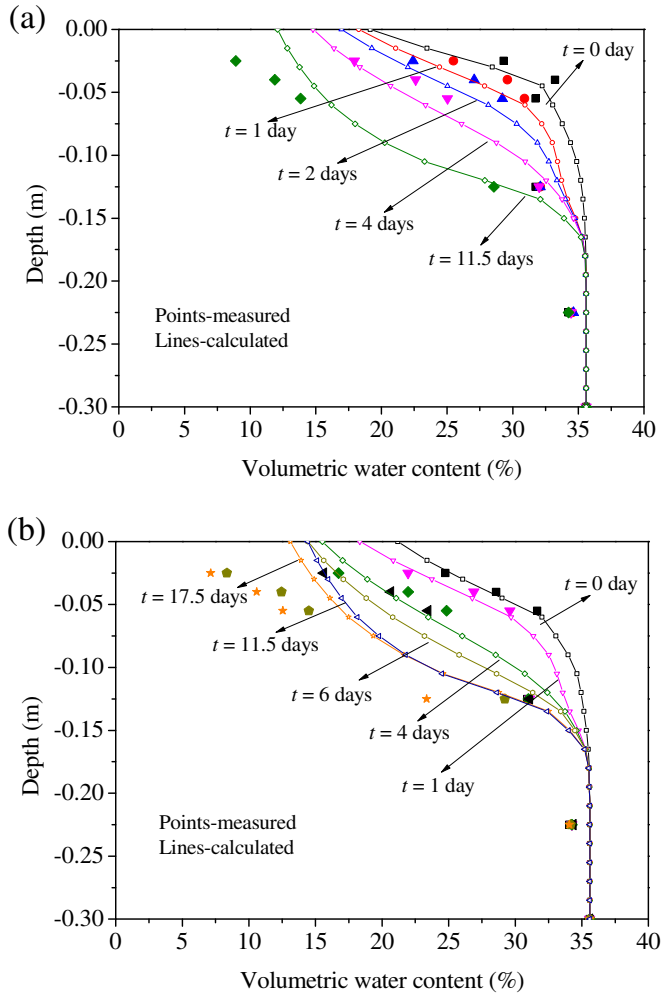


**Fig. 8.** Comparisons between the calculated and measured soil volumetric water content profiles at different moments: (a) at $t$ = 0, 1, 2, 4 and 11.5 days in Test 1; (b) at $t$ = 0, 1, 4, 6, 11.5 and 17.5 days in Test 3.

also be divided into two phases: declining phase $t$ = 0–2 days and rebounding phase $t$ = 2–11.5 days in Test 1 (Fig. 7a), declining phase $t$ = 0–6 days and rebounding phase $t$ = 6–17.5 days in Test 3 (Fig. 7b).

As mentioned previously, the measurements of soil temperature at the moment $t$ = 0 day correspond to the initial condition. In the first declining phase of Test 1, the calculated soil surface temperature declines quickly from the initial value of 13.51 °C to 11.47 °C at the second day. In the deep region, the average calculated soil temperature goes down from the initial value of 17.93 °C to 15.43 °C at $t$ = 2 days. As far as the rebounding phase is concerned, the calculated value of soil surface temperature shows an increasing tendency, varying gradually from 11.47 °C at $t$ = 2 days to 13.81 °C at $t$ = 11.5 days. The increasing tendency is also observed in the variations of the average soil temperature in the deep region, increasing from 15.43 °C at $t$ = 2 days to 16.71 °C at $t$ = 11.5 days. Similar variations for the near surface region (0 to − 0.025 m) and the deep region (− 0.025 to − 0.300 m) can also be observed in Test 3 (Fig. 7b): a declining phase is followed by a rebounding phase.

In Tests 1 and 3, an overall satisfactory agreement can be observed between the calculated and measured data in terms of soil temperature, albeit some minor differences. Fig. 7a and b show that the calculated soil temperatures at the surface point are a little larger than the measured data in the second phase of Tests 1 and 3.

Fig. 8a and b illustrate the evolutions of soil volumetric water content in Tests 1 and 3, revealing an overall consistency between the calculation and measurement results. Both of them show a continuous decrease as a result of evaporation. Note that a water tank was connected to the bottom of soil sample during the whole test, keeping the soil bottom boundary in a saturated situation. It can be identified that the soil volumetric water content in the region near the soil surface decreases more quickly than that in the deep region. However, there is no comparison of soil volumetric water content at the surface point due to the absence of measurements. Specifically, the calculated temperatures fit well with the measured data in the first two days of Test 1 and the first six days of Test 3, then deviate more afterwards. The calculated values are larger than the measured ones, indicating that more water is allowed to be transported to the surface region since day 6 to day 17.5. The differences observed may be related to the assumed soil hydraulic conductivities and soil water retention curve.

### 5.2. Test 2 and test 4

The evolutions of the soil temperature profiles in Tests 2 and 4 are presented in Fig. 9a and b, respectively. In Test 2, the initial condition is set based on the measurements at day 0, presenting a steady temperature distribution around 18.20 °C. Test 4 presents a steady temperature distribution around 20.40 °C, but with a surface temperature around 18.80 °C.

During the studied periods, the soil temperature shows a continuous increase in these two tests. In Test 2, at the surface point, the measured

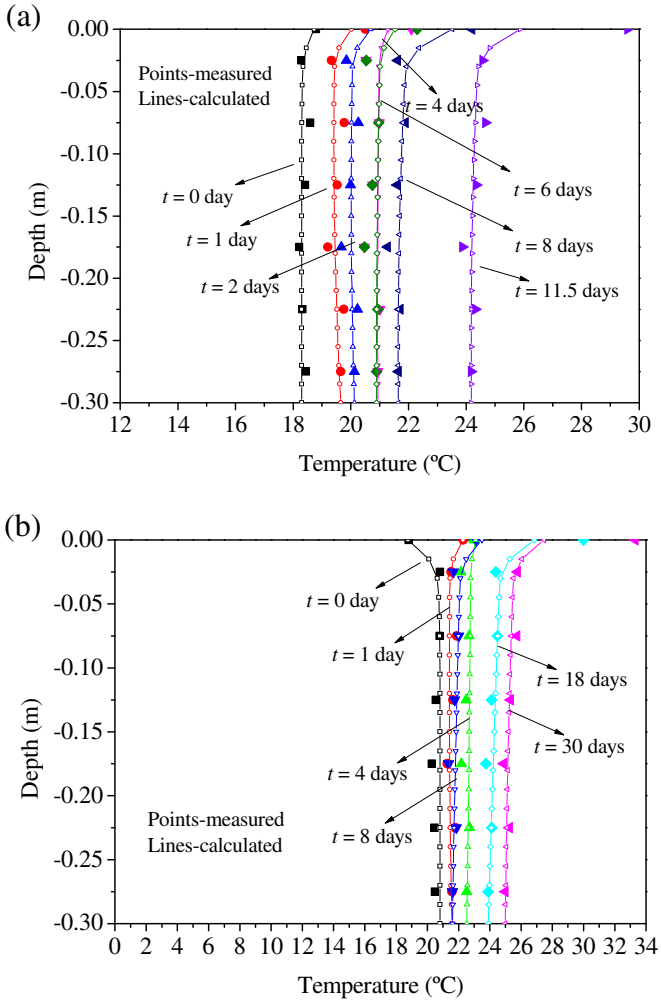


**Fig. 9.** Comparisons between the calculated and measured soil temperature profiles at different moments: (a) at $t$ = 0, 1, 2, 4, 6, 8 and 11.5 days in Test 2; (b) at $t$ = 0, 1, 4, 8, 18 and 30 days in Test 4.

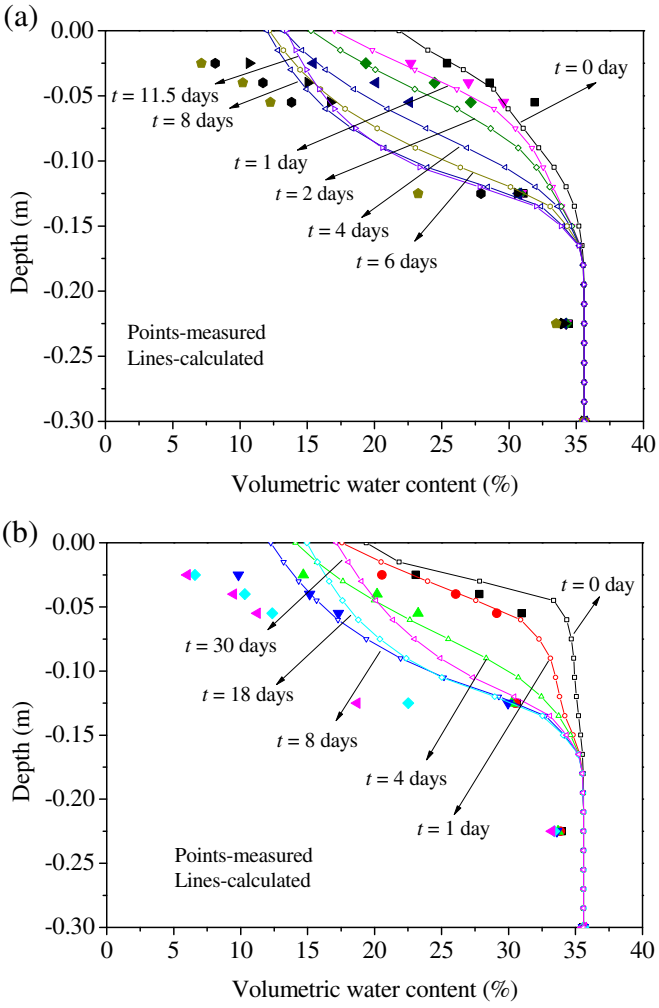


**Fig. 10.** Comparisons between the calculated and measured soil volumetric water content profiles at different moments: (a) at $t$ = 0, 1, 2, 4, 6, 8 and 11.5 days in Test 2; (b) at $t$ = 0, 1, 4, 8, 18 and 30 days in Test 4.

soil temperature increases gradually from 18.80 °C at $t$ = 0 day to 29.60 °C at $t$ = 11.5 days. For the deep region (− 0.025 to − 0.300 m), the average soil temperature at different moments varies from 18.21 °C at $t$ = 0 day to 23.87 °C at $t$ = 11.5 days. Specifically, it is noticed that the surface soil temperature rises up more quickly than those at deeper points, showing a larger soil temperature gradient in the near surface region (0 to − 0.025 m) compared to that in deep region (− 0.025 to − 0.300 m). The similar variations of soil temperature can be found in Test 4.

Overall, the calculations show a consistent variation tendency with the measurements in Tests 2 and 4. It is identified that the calculated temperatures at soil surface become lower than the measured ones from day 4 in Test 2 and from day 18 in Test 4 until the end of the test. This is to be attributed to the differences between the estimated and actual heat transfer in the near surface region: In Tests 2 and 4, sensible heat contributes to both the evaporation and soil heating. In numerical modelling, the estimated value of sensible heat is related intimately with high air temperature. During the test, the recorded air temperature in the environmental chamber may be affected by the ambient temperature (about 20 °C). As a result, the estimated sensible heat may differ from its real values in the tests, leading to lower soil surface temperatures than the measured values.

Fig. 10a and b show the consistent tendency of soil volumetric water content variations between calculation and measurement in Tests 2 and 4, respectively. However, the comparison is not conducted for the surface point due to the absence of measured data. Along with the saturated condition at the bottom of sample, the soil volumetric water distribution in the soil sample is mainly controlled by the surface evaporation. Thereby, the soil volumetric water content at the near surface region decreases more quickly than in the deep region. In Test 2, some differences are identified since day 6: the measured data shows a continuous decrease, while the calculated results decline at one moment and then start to go up. This phenomenon suggests that more water is supplied by deep region after day 6. For instance, the calculated soil surface volumetric water content at $t$ = 11.5 days is 13.43%, larger than 11.99% at $t$ = 8 days. Similar variations are observed in Test 4 (Fig. 10b), as evaporation continues, the calculated soil volumetric water content begins to show larger values than the measured data, suggesting that more water is transferred from deep region than in the real situation.

## 6. Discussions

In the four tests, it is observed that under evaporation, the soil volumetric water content keeps a decreasing tendency, whilst the soil temperature varies following different modes: two-phases (declining and rebounding phases) in Tests 1 and 3; one-phase (continuous increasing) in Tests 2 and 4. The general agreement between the measurements and calculations for both soil temperature and volumetric water content validates the numerical approaches adopted.

### 6.1. The evaporation stages and soil temperature

In literature, a general three-stage evaporation process was concluded: constant-rate stage, falling-rate stage and slow-rate stage (Yanful and Choo, 1997; Hillel, 2004; Lal and Shukla, 2005; Qiu and Ben-Asher, 2010; An, 2017). This process was identified under three conditions:

i) A continual energy supply to support evaporation;
ii) The existence of a vapor pressure gradient between the evaporating surface and atmosphere;
iii) A continual supply of water from the interior of soil to the evaporating surface.

In this study, the evaporation process was recorded for 11.5 days, 11.5 days, 17.5 days and 30 days in Test 1, Test 2, Test 3 and Test 4, respectively. More precisely, two stages of evaporation process can be identified in Test 1 (Fig. 6a): first falling stage (0–2 days) and constant-rate stage (2–11.5 days). Fig. 6c reveals three stages of evaporation process in Test 3: first falling stage (0–6 days), constant-rate stage (6–11.5 days) and slow-rate stage (11.5–17.5 days). On the other hand, three-stages are also observed in Test 2 (Fig. 6b) and Test 4 (Fig. 6d): the evaporation in Test 2 consists of a constant-rate stage (0–6 days), a falling-rate stage (6–10 days) and a slow-rate stage (10–11.5 days); the evaporation in Test 4 involves a constant-rate stage (0–6 days), a falling-rate stage (6–14 days) and a slow-rate stage (14–30 days). Consequently, a special falling rate stage during the periods of 0–2 days and 0–6 days is identified in Tests 1 and 3 respectively before the general first stage of evaporation. This special stage is most likely caused by the non-sufficient supply of evaporative energy (inconformity of condition i). As the air temperature is low (heating tube temperatures 50 °C) in Tests 1 and 3, it is impossible to keep the evaporation at a rate as high as the initial value, leading to the sudden drop of evaporation rate.

In terms of soil temperature variations, the measurements and calculations of three points P1, P2, and P3 at different depths of 0 mm, 75 mm, and 225 mm in four tests are drawn respectively in Fig. 11. Two phases are identified in Test 1 (Fig. 11a) and Test 3 (Fig. 11c): a declining phase and a rebounding phase. Along with the first falling stage of evaporation, the soil temperature decreases firstly, reaching the minimum value at the end of the first phase. In the second phase, the soil temperature starts to go up, approaching the initial temperature at the end of test. The turning points of these two phases in Tests 1 and 3 are at day 2 and day 6, respectively. Correspondingly, soil temperature at different depths in Tests 1 and 3 reach their minimum values at day 2 and day 6, respectively. In Test 2 (Fig. 11b) and Test 4 (Fig. 11d), the soil temperature shows continuous increases, corresponding to the conventional three stages of evaporation during the studied periods (Fig. 6b and Fig. 6d).

Indeed, soil temperature variation is mainly governed by the soil heat flux boundary condition which depends on the variations of sensible heat and latent heat, so that soil temperature is intimately related to the evaporation. In Test 1 (Fig. 6a) and Test 3 (Fig. 6c), in the first falling stage of evaporation, low air temperature cannot provide sufficient energy to support evaporation at its initial value. It can be inferred that evaporation takes energy from both air and soil hence the soil temperature decreases gradually. In other words, the value of the latent heat is equal to the sum of sensible and soil heat so that latent heat influences the evaporation more significantly during the periods of 0–2 days in Test 1 and 0–6 days in Test 3. Afterwards, air provides enough energy to the evaporation that happens at lower rates, indicating that air is able to provide sufficient energy for both evaporation and soil heating. This suggests that the sensible heat is partitioned into latent heat and soil heat, governing the evaporation more predominantly. Thereby, the soil temperatures at different depths show continuous increases in the following days. In Tests 2 and 4 (Fig. 6b and Fig. 6d respectively), evaporation continues following three-stages and the soil temperature at different depths show continuous increases. It is inferred that the process of evaporation is ensured by sufficient energy from air at high temperature in these two tests. In other words, sensible heat governs the evaporation more predominantly during the whole periods of Tests 2 and 4.

Note that heat convection is not included in the heat flow due to its importance of second order compared with conduction and latent heat. However, the values of convection may go up as the increase of soil temperature gradient in the near surface region during evaporation. Thereby, neglecting convection in the heat transfer may partly explain the difference of soil temperature between the calculations and measurements at the end of each test, especially the surface soil temperature of Tests 2 and 4.

In conclusion, the mode of soil temperature variations is related intimately with the evaporation process and is proposed to be estimated by identifying the actual evaporation curve. Generally, the first declining phase of soil temperature accompanied with the following rebounding phase normally occurs with the appearance of sudden first-falling stage of evaporation as presented in Tests 1 and 3. Moreover, in the two-phases of soil temperature variations as presented in Tests 1 and 3, soil temperatures at different depths reach their minimum values at the starting time of the constant-stage of evaporation. The continuous increasing tendency of soil temperature is observed along with three-stages of evaporation as the cases of Tests 2 and 4.

### 6.2. Dry layer

As evaporation continues, the surface sand can become dry, forming a dry layer in the near surface zone (Song et al., 2013, 2014; Song, 2014). Consequently, the evaporation front will move to the bottom of the dry layer as presented in Fig. 12. In that case, the soil water evaporation presents three stages (Aluwihare and Watanabe, 2003): (1) water vapor is carried out from the water surface to the bottom of dry layer, (2) water vapor is transported from the bottom of dry soil layer to the soil surface by vapor diffusion and (3) water vapor travels from the soil surface to atmosphere.

With the appearance of dry layer, soil properties in this region vary, giving rise to the location change of the actual top water flux boundary condition. Owing to the absence of soil volumetric water content measurements in this zone, it is difficult to determine the variations of the dry layer depth. In the numerical modelling conducted, the effect of this dry layer is not considered and the evaporation front is assumed to be on the top of soil surface during the whole studied period. As a result, the numerical results may be affected by this ignorance and this may be another reason for the differences between the calculations and measurements at the end of each test. This aspect will be further investigated.

## 7. Conclusions

In an attempt to assess the increasing influence of climate change and global warming on earth structures, a numerical approach combining a coupled hydro-thermal model and a soil-atmosphere interaction model is developed to investigate the variations of soil temperature and water content during evaporation. Four different evaporation tests of Fontainebleau sand in an experimental environmental chamber are investigated, showing the relevance of the proposed numerical approach.

The variations of soil temperature and volumetric water content as well as the water and heat flux boundary conditions at the soil top surface in the four evaporation tests are analyzed in-depth. It is observed that the soil volumetric water content keeps a continuous decreasing tendency due to the evaporation on soil surface. However, during evaporation, soil temperature presents two variation modes depending on the top heat flux boundary conditions: two-phases

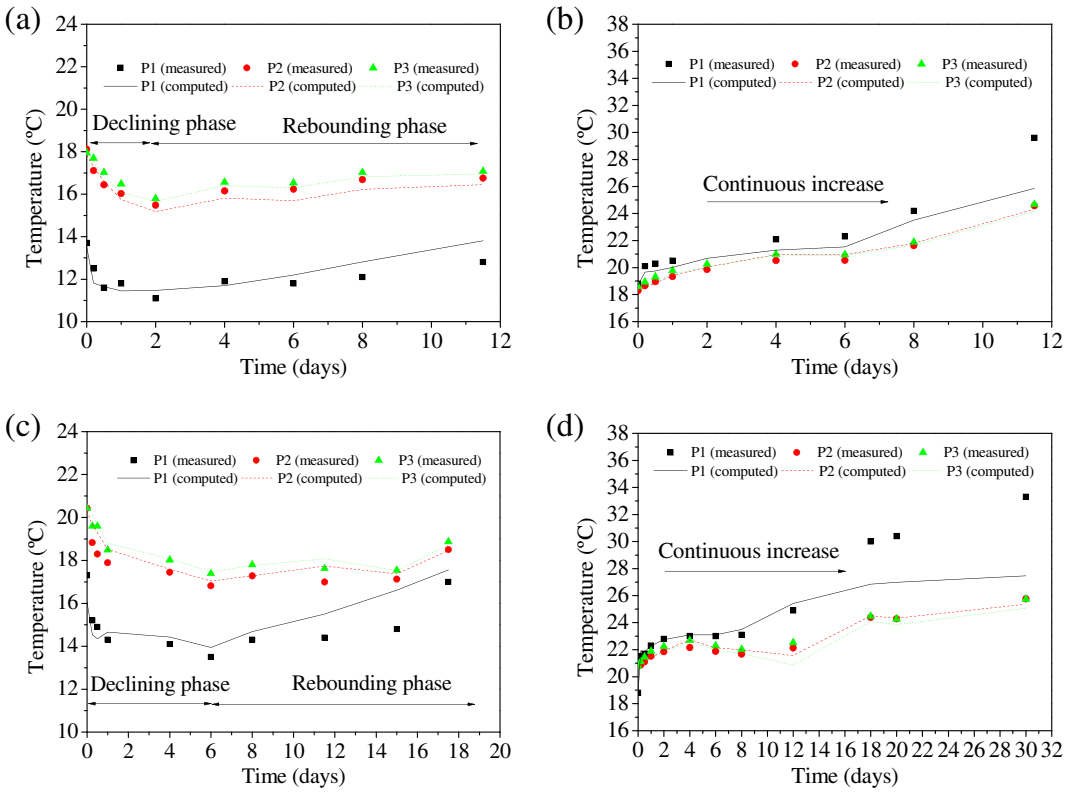


**Fig. 11.** The comparisons between the calculated and measured soil temperature versus time at Points P1, P2 and P3: (a) Test 1; (b) Test 2; (c) Test 3; (d) Test 4.

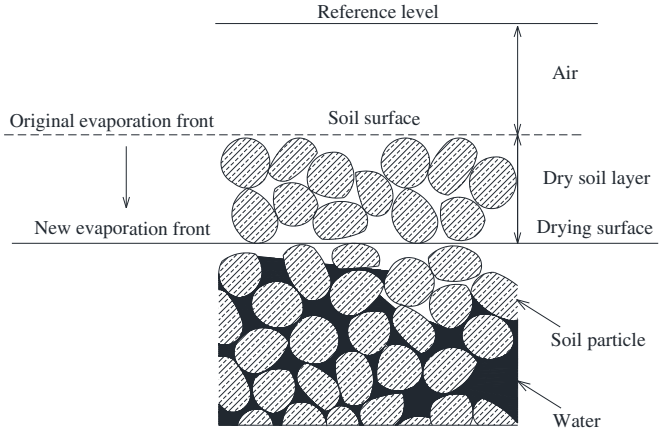


**Fig. 12.** Diagram of dry soil layer in the evaporation process (modified after Aluwihare and Watanabe, 2003 and Song, 2014).

(declining and rebounding phases) in Tests 1 and 3; one-phase (continuous increase) in Tests 2 and 4. The mode of soil temperature variations is proposed to be estimated directly based on the observed actual evaporation curve. Two phases of soil temperature variations are identified in the case of appearance of a sudden first-falling stage of evaporation. Specifically, the moment of soil surface temperature reaching the minimum value corresponds to the starting time of the constant-stage of evaporation in this case. However, only one phase of soil temperature variations is observed in the common three-stage evaporation case without the sudden first-falling stage.

## Nomenclature

| | |
|---|---|
| $C$ | Volumetric heat capacity of the soil (J/(m$^3$K)) |
| $C_{T\varphi}$ | Volumetric isothermal capacity of the structure (J/m$^4$) |
| $C_T$ | Volumetric thermal capacity of the structure (J/(m$^3$K)) |
| $C_{\varphi T}$ | Volumetric thermal capacity of moisture (kg/(m$^3$K)) |
| $C_\varphi$ | Volumetric isothermal capacity of moisture (kg/m$^4$) |
| $C_{pl}$ | Specific heat capacity of water liquid (J/(kgK)) |
| $C_{ps}$ | Specific heat capacity of soil solid (J/(kgK)) |
| $C_{pv}$ | Specific heat capacity of water vapor (J/(kgK)) |
| $C_{pa}$ | Specific heat capacity of air (J/(kgK)) |
| $D_{atm}$ | Molecular diffusivity of the pore vapor (m$^2$/s) |
| $D_{TV}$ | Thermal vapor diffusivity (m$^2$/(sK)) |
| $D_{\varphi V}$ | Isothermal vapor diffusivity (m/s) |
| $E_a$ | Actual evaporation rate (m/s) |
| $G$ | Soil heat flux (W/m$^2$) |
| $H$ | Sensible heat flux (W/m$^2$) |
| $h_{a\text{-outlet}}$ | Absolute humidity values at the outlet of environmental chamber (Mg/m$^3$) |
| $h_{a\text{-inlet}}$ | Absolute humidity values at the inlet of environmental chamber (Mg/m$^3$) |
| $K_H$ | Eddy diffusivity for heat through air (m$^2$/s) |
| $K_T$ | Thermal soil structure diffusivity (W/(mK)) |
| $K_{T\varphi}$ | Isothermal soil structure diffusivity (W/m$^2$) |
| $K_{\varphi T}$ | Thermal moisture diffusivity (kg/(msK)) |
| $K_\varphi$ | Isothermal moisture diffusivity (kg/(sm$^2$)) |
| $K$ | Unsaturated soil hydraulic conductivity (m/s) |
| $K_s$ | Saturated soil hydraulic conductivity (m/s) |
| $L_E$ | Latent heat flux (W/m$^2$) |
| $L_v$ | Latent heat of vaporization of water (J/kg) |
| $Q$ | Air flow rate through the chamber (L/s) |
| $T_a$ | Air temperature (°C) |
| $\alpha$ | Tortuosity factor for soil |
| $\beta$ | Cross-sectional area of the soil that is available for vapor flow |
| $\theta$ | Volumetric water content |
| $\theta_s$ | Saturated volumetric water content |
| $\theta_r$ | Residual volumetric water content |
| $\varphi$ | Hydraulic head (m) |

| | |
|---|---|
| $\lambda$ | Thermal conductivity of soil (W/(mK)) |
| $\rho_0$ | Density of saturated water vapor (kg/m$^3$) |
| $\rho_l$ | Density of water liquid (kg/m$^3$) |
| $\rho_v$ | Density of water vapor (kg/m$^3$) |

## Acknowledgements

The authors wish to acknowledge the support of the European Commission by the Marie Curie IRSES project GREAT - Geotechnical and geological Responses to climate change: Exchanging Approaches and Technologies on a world-wide scale (FP7-PEOPLE-2013-IRSES-612665). The authors also wish to thank the China Scholarship Council (CSC) and Ecole des Ponts ParisTech for their financial supports.

## Reference

Aluwihare, S., Watanabe, K., 2003. Measurement of evaporation on bare soil and estimating surface resistance. J. Environ. Eng. 129, 1157–1168. http://dx.doi.org/10.1061/(ASCE)0733-9372(2003)129:12(1157.

An, N., 2017. Numerical Investigation of Soil-Atmosphere Interaction: Application to Embankments of Treated Soils. PhD thesis. Université Paris-Est, Paris.

Bittelli, M., Ventura, F., Campbell, G.S., Snyder, R.L., Gallegati, F., Pisa, P.R., 2008. Coupling of heat, water vapor, and liquid water fluxes to compute evaporation in bare soils. J. Hydrol. 362, 191–205. http://dx.doi.org/10.1016/j.jhydrol.2008.08.014.

Blight, G.E., 1997. Interactions between the atmosphere and the Earth. Geotechnique 47, 715–767. http://dx.doi.org/10.1680/geot.1997.47.4.713.

Buongiorno, J., Venerus, D.C., Prabhat, N., McKrell, T., Townsend, J., Christianson, R., Tolmachev, Y.V., Keblinski, P., Hu, L.W., Alvarado, J.L., Bang, I.C., Bishnoi, S.W., Bonetti, M., Botz, F., Cecere, A., Chang, Y., Chen, G., Chen, H., Chung, S.J., Chyu, M.K., Das, S.K., Di Paola, R., Ding, Y., Dubois, F., Dzido, G., Eapen, J., Escher, W., Funfschilling, D., Galand, Q., Gao, J., Gharagozloo, P.E., Goodson, K.E., Gutierrez, J.G., Hong, H., Horton, M., Hwang, K.S., Iorio, C.S., Jang, S.P., Jarzebski, A.B., Jiang, Y., Jin, L., Kabelac, S., Kamath, A., Kedzierski, M.A., Kieng, L.G., Kim, C., Kim, J.H., Kim, S., Lee, S.H., Leong, K.C., Manna, I., Michel, B., Ni, R., Patel, H.E., Philip, J., Poulikakos, D., Reynaud, C., Savino, R., Singh, P.K., Song, P., Sundararajan, T., Timofeeva, E., Tritcak, T., Turanov, A.N., Van Vaerenbergh, S., Wen, D., Witharana, S., Yang, C., Yeh, W.H., Zhao, X.Z., Zhou, S.Q., 2009. A benchmark study on the thermal conductivity of nanofluids. J. Appl. Phys. 106. http://dx.doi.org/10.1063/1.3245330.

Côté, J., Konrad, J.-M., 2005. A generalized thermal conductivity model for soils and construction materials. Can. Geotech. J. 42, 443–458. http://dx.doi.org/10.1139/t04-106.

Cui, Y.J., Lu, Y.F., Delage, P., Riffard, M., 2005. Field simulation of in situ water content and temperature changes due to ground–atmospheric interactions. Géotechnique 55, 557–567. http://dx.doi.org/10.1680/geot.2005.55.7.557.

Cui, Y.J., Gao, Y.B., Ferber, V., 2010. Simulating the water content and temperature changes in an experimental embankment using meteorological data. Eng. Geol. 114, 456–471. http://dx.doi.org/10.1016/j.enggeo.2010.06.006.

Cui, Y.J., Ta, A.N., Hemmati, S., Tang, A.M., Gatmiri, B., 2013. Experimental and numerical investigation of soil-atmosphere interaction. Eng. Geol. 165, 20–28. http://dx.doi.org/10.1016/j.enggeo.2012.03.018.

Delfosse-Ribay, E., Djeran-Maigre, I., Cabrillac, R., Gouvenot, D., 2004. Shear modulus and damping ratio of grouted sand. Soil Dyn. Earthq. Eng. 24, 461–471. http://dx.doi.org/10.1016/j.soildyn.2004.02.004.

Doussan, C., Ruy, S., 2009. Prediction of unsaturated soil hydraulic conductivity with electrical conductivity. Water Resour. Res. 45, 1–12. http://dx.doi.org/10.1029/2008WR007309.

Gerard, P., Charlier, R., Chambon, R., Collin, F., 2008. Influence of evaporation and seepage on the convergence of a ventilated cavity. Water Resour. Res. 44, W00C02. http://dx.doi.org/10.1029/2007WR006500.

Gitirana Jr., G.D.F.N., 2005. Weather-Related Geo-Hazard Assessment Model for Railway Embankment Stability.

Gitirana, G., Fredlund, M.D., Fredlund, D.G., 2006. Numerical modelling of soil-atmosphere interaction for unsaturated surfaces. In: Proc. the 4th International Conference on Unsaturated Soils, Arizona, pp. 658–669.

Grifoll, J., Gastó, J.M., Cohen, Y., Gast??, J.M., Cohen, Y., 2005. Non-isothermal soil water transport and evaporation. Adv. Water Resour. 28, 1254–1266. http://dx.doi.org/10.1016/j.advwatres.2005.04.008.

Hansson, K., Lundin, L.-C., Šimůnek, J., 2005. Modeling water flow patterns in flexible pavements. Transp. Res. Rec. 1936, 131–141. http://dx.doi.org/10.3141/1936-16.

Hecht, F., 2010. FreeFem + +, a Tool to Solve PDE's Numerically.

Hillel, D., 2004. Introduction to environmental soil physics. Energy 337–348 (chapter 18).

Kondo, J., Saigusa, N., Sato, T., 1992. A model and experimental study of evaporation from bare-soil surfaces. J. Appl. Meteorol. http://dx.doi.org/10.1175/1520-0450(1992)031<0304:AMAESO>2.0.CO;2.

Lal, R., Shukla, M.K., 2005. Principles of Soil Physics. The Ohio State University, Columbus, Ohio, U.S.A.

Lee, I.-M., Lee, H.-J., Cheon, J.-Y., Reddi, L.N., 2003. Evaporation theory for deformable soils. J. Geotech. Geoenviron. 129, 1020–1027. http://dx.doi.org/10.1061/(ASCE)1090-0241(2003)129:11(1020.

Leung, A., Ng, C., 2013. Analyses of groundwater flow and plant evapotranspiration in a vegetated soil slope. Can. Geotech. J. 1218, 1204–1218. http://dx.doi.org/10.1139/cgj-2013-0148.

Mbonimpa, M., De Montréal, É.P., Bédard, C., Aubertin, M., Bussière, B., 2004. A Model To Predict the Unsaturated Hydraulic. (geo quebec meeting 16–23).

Philip, J.R., De Vries, D.A., 1957. Moisture movements in porous materials under temperature gradients. EOS Trans. Am. Geophys. Union 38, 222–232.

Qiu, G.Y., Ben-Asher, J., 2010. Experimental determination of soil evaporation stages with soil surface temperature. Soil Sci. Soc. Am. J. 74, 13. http://dx.doi.org/10.2136/sssaj2008.0135.

Rahardjo, H., Satyanaga, A., Leong, E.C., 2013. Effects of flux boundary conditions on pore-water pressure distribution in slope. Eng. Geol. 165, 133–142. http://dx.doi.org/10.1016/j.enggeo.2012.03.017.

Rayhani, M.H.T., Yanful, E.K., Fakher, A., 2007. Desiccation-induced cracking and its effect on the hydraulic conductivity of clayey soils from Iran. Can. Geotech. J. 44, 276–283. http://dx.doi.org/10.1139/t06-125.

Rykaart, M., Fredlund, M., Stianson, J., 2001. Solving tailings impoundment water balance problems with 3-D seepage software. Geotech. News 50–55 (December).

Smits, K.M., Cihan, A., Sakaki, T., Illangasekare, T.H., 2011. Evaporation from soils under thermal boundary conditions: experimental and modeling investigation to compare equilibrium- and nonequilibrium-based approaches. Water Resour. Res. 47, 1–14. http://dx.doi.org/10.1029/2010WR009533.

Song, W.K., 2014. Experimental Investigation of Water Evaporation from Sand and Clay Using an Environmental Chamber. Université Paris-Est, Paris.

Song, W.-K., Cui, Y.-J., Tang, A.M., Ding, W.-Q., Tran, T.D., 2013. Development of a large-scale environmental chamber for investigating soil water evaporation. Geotech. Test. J. 36, 20120142. http://dx.doi.org/10.1520/GTJ20120142.

Song, W.-K., Cui, Y.-J., Tang, A.M., Ding, W.-Q., Tran, T.D., 2014. Experimental study on water evaporation from sand using environmental chamber. Can. Geotech. J. 51, 115–128. http://dx.doi.org/10.1139/cgj-2013-0155.

Swanson, D.A., Barbour, S.L., Wilson, G.W., O'Kane, M., 2003. Soil–atmosphere modelling of an engineered soil cover for acid generating mine waste in a humid, alpine climate. Can. Geotech. J. 40, 276–292. http://dx.doi.org/10.1139/t02-116.

Ta, A.-N., 2009. Etude de l ' interaction sol-atmosphère en chambre environnementale. Université Paris-Est.

Tang, A.-M., Cui, Y.-J., 2007. Controlling Suction by Vapour Equilibrium Technique at Different Temperatures, Application to the Determination of the Water Retention Properties of MX80 Clay. Vol. 10. pp. 1–10. http://dx.doi.org/10.1139/T04-082.

Tang, C.S., Cui, Y.J., Tang, A.M., Shi, B., 2010. Experiment evidence on the temperature dependence of desiccation cracking behavior of clayey soils. Eng. Geol. 114, 261–266. http://dx.doi.org/10.1016/j.enggeo.2010.05.003.

Tang, C.S., Cui, Y.J., Shi, B., Tang, A.M., Liu, C., 2011. Desiccation and cracking behaviour of clay layer from slurry state under wetting-drying cycles. Geoderma 166, 111–118. http://dx.doi.org/10.1016/j.geoderma.2011.07.018.

Tang, C.S., Shi, B., Cui, Y.J., Liu, C., Gu, K., 2012. Desiccation cracking behavior of polypropylene fiber–reinforced clayey soil. Can. Geotech. J. 49, 1088–1101. http://dx.doi.org/10.1139/t2012-067.

Teng, T.P., Hung, Y.H., Teng, T.C., Mo, H.E., Hsu, H.G., 2010. The effect of alumina/water nanofluid particle size on thermal conductivity. Appl. Therm. Eng. 30, 2213–2218. http://dx.doi.org/10.1016/j.applthermaleng.2010.05.036.

Thomas, H.R., King, S.D., 1991. Coupled temperature/capillary potential variations in unsaturated soil. J. Eng. Mech. http://dx.doi.org/10.1061/(ASCE)0733-9399(1991)117:11(2475.

van Genuchten, M.T.T., 1980. A closed-form equation for predicting the hydraulic conductivity of unsaturated Soils1. Soil Sci. Soc. Am. J. 44, 892–898. http://dx.doi.org/10.2136/sssaj1980.03615995004400050002x.

Wilson, G.W., 1990. Soil Evaporation Fluxes for Geotechnical Engineering Problems. PhD thesis. University of Saskatchewan, Saskatoon.

Wilson, G.W., Machibroda, R.T., Barbour, S.L., Woyshner, M.R., 1993. Modelling of soil evaporation from waste disposal sites. In: Proceedings of the Joint CSCE-ASCE National Conference on Environmental Engineering. Montreal, pp. 281–288.

Wilson, G.W., Fredlund, D.G., Barbour, S.L., 1994. Coupled soil-atmosphere modelling for soil evaporation. Can. Geotech. J. 31, 151–161. http://dx.doi.org/10.1139/t94-021.

Yamanaka, T., Inoue, M., Kaihotsu, I., 2004. Effects of gravel mulch on water vapor transfer above and below the soil surface. Agric. Water Manag. 67, 145–155. http://dx.doi.org/10.1016/j.agwat.2004.01.002.

Yanful, E.K., Choo, L.-P., 1997. Measurement of evaporative fluxes from candidate cover soils. Can. Geotech. J. 34, 447–459. http://dx.doi.org/10.1139/t97-002.

Yanful, E.K., Simms, P.H., Rowe, R.K., Stratford, G., 1999. Monitoring an experimental soil waste near London, Ontario, Canada. Geotech. Geol. Eng. 17, 65–84. http://dx.doi.org/10.1023/A:1008986103460.

Yanful, E.K., Mousavi, S.M., Yang, M., 2003. Modeling and measurement of evaporation in moisture-retaining soil covers. Adv. Environ. Res. 7, 783–801. http://dx.doi.org/10.1016/S1093-0191(02)00053-9.

Yang, M.K., Yanful, E., 2002. Water balance during evaporation and drainage in cover soils under different water table conditions. Adv. Environ. Res. 6, 505–521. http://dx.doi.org/10.1016/S1093-0191(01)00077-6.

Zhai, X.M., Greatbatch, R.J., 2006. Surface eddy diffusivity for heat in a model of the northwest Atlantic Ocean. Geophys. Res. Lett. 33, L24611. http://dx.doi.org/10.1029/2006GL028712.